Stochastic cell-intrinsic stem cell decisions control colony growth in planarians

Tamar Frankovits[1], Prakash Varkey Cherian[1], Yarden Yesharim[1], Simon Dobler[1,2], Omri Wurtzel[1,3]

[1] The School of Neurobiology, Biochemistry & Biophysics, George S. Wise Faculty of Life Sciences, Tel Aviv University, Tel Aviv, Israel

[2] Present address: Interfaculty Institute of Microbiology and Infection Medicine, University of Tübingen, Tübingen, Germany

[3] Sagol School of Neuroscience, Tel Aviv University, Tel Aviv, Israel

* Correspondence: owurtzel@tauex.tau.ac.il

Abstract

Stem cells contribute to organismal homeostasis by balancing division, self-renewal and differentiation. Elucidating the strategies by which stem cells achieve this balance is critical for understanding homeostasis, and for addressing pathogenesis associated with the disruption of this balance (e.g., cancer). Planarians, highly regenerative flatworms, use pluripotent stem cells called neoblasts to maintain and regrow organs. A single neoblast can rescue an entire animal depleted from stem cells and regenerate all cell lineages. How neoblast differentiation and clonal expansion are governed to produce all the required cell types is unclear. Here, we integrated experimental and computational approaches to develop a quantitative model revealing basic principles of clonal growth of individual neoblasts. By experimentally suppressing differentiation to major lineages, we elucidated the interplay between colony growth and lineage decisions. Our findings suggest that neoblasts pre-select their progenitor lineage based on a cell-intrinsic fate distribution. Arresting differentiation into specific lineages disrupts neoblast proliferative capacity without inducing compensatory expression of other lineages. Our analysis of neoblast colonies is consistent with a cell-intrinsic decision model that can operate without memory or communication between neoblasts. This simple cell fate decision process breaks down in homeostasis, likely because of the activity of feedback mechanisms. Our findings uncover essential principles of stem cell regulation in planarians, which are distinct from those observed in many vertebrate models. These mechanisms enable robust production of diverse cell types, and facilitate regeneration of missing tissues.

Introduction

Stem cells are crucial for achieving and maintaining homeostasis. Paradoxically, they contribute to an organism's equilibrium through highly dynamic behavior, continuously balancing their population size by regulating rates of self-renewal and differentiation. Understanding the strategies used to accomplish this balance can provide the key to elucidating organismal homeostasis, as well as to modeling pathogenesis associated with disruption to this balance (e.g., cancer) (Passegué et al., 2003; Singh et al., 2011).

Valuable insights into stem cell behavior can be derived from studying systems that rely on principles differing significantly from those characterizing vertebrate stem cells. Neoblasts, the pluripotent stem cells in planarians, function in tissue regeneration and maintenance, providing an intriguing platform in this regard. Neoblasts avoid quiescence, and quickly adapt to changes in organismal requirements by adjusting the quantities and types of cells they produce (González-Estévez et al., 2012; Wagner et al., 2011). These strategies challenge fundamental concepts of vertebrate stem cells. For example, in adult vertebrates, hematopoietic stem cells typically divide slowly, giving rise to rapidly dividing transit amplifying cells forming tissue-specific progenitors (Abkowitz et al., 2000; Becker et al., 2006). These progenitors bear the primary responsibility for maintaining homeostasis. Planarian neoblasts, by contrast, divide rapidly and do not employ transit amplifying cells for progeny production (Pearson, 2022; Raz et al., 2021; van Wolfswinkel et al., 2014). Moreover, neoblasts do not seem to retain memory of the progeny cell types they generate (Raz et al., 2021; van Wolfswinkel et al., 2014). Notably, despite being essentially ageless and immortal, neoblasts do not display cancerous-like states (Van Roten et al., 2018). Therefore, elucidating how neoblasts balance self-renewal and differentiation can contribute to understanding fundamental strategies that facilitate tissue homeostasis and regeneration of lost or damaged tissues (Levin et al., 2019).

Prior modeling of neoblast dynamics in planarians has produced a valuable analytical framework for studying the dynamics of the entire neoblast system (Mangel et al., 2016). However, analyzing isolated neoblasts and their progeny can be instrumental for understanding how decisions are made at a single cell resolution, as well as for deriving physiological parameter values (e.g., corresponding to proliferation and differentiation) that are relevant to the larger system. *In vivo* analysis of individual neoblasts and their progeny is often achieved by applying subtotal irradiation to whole planarians, which results in near-complete neoblast ablation (Wagner et al., 2011). Surviving neoblasts proliferate to form distinct colonies,

allowing analysis of growth dynamics and progeny identity (Lei et al., 2016; Wagner et al., 2012). Though such analysis has been instrumental in uncovering regulators of proliferation and differentiation (Wagner et al., 2012), a quantitative analysis of neoblast colony growth that integrates these principles has yet to be established and experimentally validated.

Several open questions need to be addressed in the development of such a model. For example, it is unclear whether neoblasts select their lineage identity in a synchronous manner or function independently (Bohr et al., 2021; Reddien, 2018). Moreover, as indicated above, it is unclear whether neoblasts maintain memory of their decisions over successive rounds of the cell cycle (Pearson, 2022). In addition, as discussed in what follows, critical knowledge is lacking regarding the ability of neoblasts to switch from producing differentiating lineage to contributing to neoblast colony growth; an understanding of this switch is fundamental for analyzing the overall development of a colony, and for describing new tissue production in regeneration.

Herein, we begin to address these gaps, integrating experimental and computational approaches to analyze neoblast colony growth. Our analysis does not assume communication between neoblasts or memory of cell fate decisions; rather, it explores whether straightforward stochastic selection of division outcome can adequately describe the growth of a neoblast colony. Based on *in vivo* analysis of neoblast clone growth, neoblast division can result in three potential outcomes (Fig 1) (Lei et al., 2016; Raz et al., 2021): (1) symmetric renewal, which generates two neoblasts; (2) symmetric differentiation, which generates two post-mitotic cells; and (3) asymmetric division, which produces a neoblast and a post-mitotic cell.

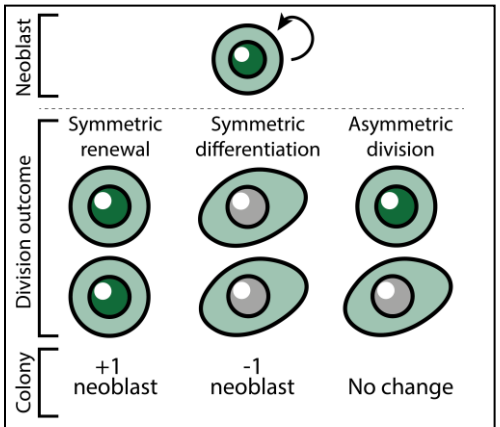

Figure 1. Potential outcomes of neoblast division and the effect on colony size

In what follows, we study and analyze colony growth based on these principles. We derive key parameter values from experimental data and show that these values predict colony growth with high accuracy. Next, in a series of experiments, we seek to uncover whether the core principles that drive neoblast colony growth (as proposed in our model) are further shaped by individual neoblasts' decisions regarding progeny lineage commitment. In particular, many S/G2/M neoblasts express fate-specifying transcription

factors (FSTFs), which direct the differentiation of their progeny into specific lineages (Reddien, 2013; Scimone et al., 2014; Zeng et al., 2018). Importantly, a neoblast can express different FSTFs in successive rounds of division, which results in production of post-mitotic progenitors of different lineages (Raz et al., 2021; van Wolfswinkel et al., 2014). Thus, the growth potential of the colony is not compromised by FSTF expression. Yet, it remains unclear how the growth of a colony might be affected when expression of a particular FSTF (and thus the corresponding cell lineage) is blocked: for example, does colony growth remain stable, with other lineages being overexpressed to compensate for the blocked lineage? Notably, our experimental perturbation analysis shows that blocking the expression of an FSTF incapacitates a proportion of neoblasts equivalent to the size of the lineage affected. This observation reveals a critical dependency: once a neoblast commits to a specific lineage, it retains this identity until cell division concludes. By contrast, inhibiting FSTFs during homeostasis resulted in an increase in the number of cycling cells, consistent with an activity of feedback mechanisms that regulate cell proliferation in homeostasis (Cheng et al., 2018; Pearson and Sánchez Alvarado, 2010).

Together, our findings imply that simple design principles govern cell fate choices in neoblast colonies, and that accurate prediction of colony growth does not require assumptions of fate-specification memory, or coordination of cell fate choices between neoblasts. Moreover, our findings suggest that all neoblasts in a colony are functionally equivalent (i.e., able to self-renew and to divide to all cell types), and elucidate the contribution of decisions in individual planarian stem cells to achieving systemic homeostasis.

Results

Analysis of neoblast colony growth

Following subtotal irradiation, a surviving neoblast may proliferate to form a colony (Fig 2A). The growing colony is the exclusive source of new cells (Wagner et al., 2012, 2011). We used an exponential growth equation to estimate the change in colony size over time of a successfully established colony by a surviving neoblast (Eq 1). The function incorporates three parameters to estimate colony growth: (1) average cell cycle length (τ); (2) symmetric renewal probability (p), where symmetric renewal rate per hour is $p' = p/\tau$; and (3) symmetric differentiation or neoblast elimination probability (q), where symmetric differentiation or neoblast elimination rate per hour is $q' = q/\tau$. Asymmetric divisions do not alter neoblast count (Fig 1).

123 $$\frac{dN}{dt} = p'N - q'N = \frac{(p-q)N}{\tau}$$

124 [1]

125 We used the solution to the equation, and included the initial colony size (N_0), to predict colony sizes (Eq
126 2) using a range of parameter values and evaluated the model predictions (Fig 2B; Fig S1) with our own
127 and published data (Raz et al., 2021; Wagner et al., 2012).

128

129 $$N(t) = N_0 e^{\frac{(p-q)t}{\tau}}$$

130 [2]

131 The plots in Figure 2B show how varying the value of growth parameters is predicted to affect colony size.
132 The cell division time (τ) has the most substantial impact on colony growth. For example, a simulated
133 colony with a fast (16 hours) cell cycle (with p and q set at 0.5 and 0, respectively) had a neoblast count
134 approximately ten times larger than that reported in literature (Lei et al., 2016; Raz et al., 2021; Wagner
135 et al., 2012, 2011; Zeng et al., 2018). To determine the average cell cycle time (τ), we re-analyzed
136 available colony growth data that had previously been experimentally obtained using bromodeoxyuridine
137 (BrdU) metabolic labeling (Lei et al., 2016). In those experiments, BrdU was incorporated into DNA during
138 both symmetric and asymmetric divisions using a pulse (4 hours) significantly shorter than the cell cycle
139 time, followed by a chase of up to 72 hours (Fig 2C). We predicted that the $BrdU^+$ cell number would grow
140 linearly until the entire population doubles. Then, completion of successive cell divisions would lead to
141 exponential growth in $BrdU^+$ cell number. Indeed, the colony growth was initially linear (Pearson r =
142 0.997), and using linear regression, we estimated that the colony doubling time, and hence the average
143 cell cycle length, was 29.7 hours (Fig 2C).

144

145 The symmetric renewal probability (p) is a vital factor in colony growth, and even slight variations in p
146 have large cumulative effects (Fig 2B). We experimentally determined the symmetric renewal probability
147 by subjecting planarians to subtotal irradiation (1750 rad; Methods) and identifying neoblasts via
148 fluorescence *in situ* hybridization (FISH) with the *smedwi-1* marker (Reddien et al., 2005b), a pan-neoblast
149 marker. We imaged pairs of adjacent *smedwi-1*$^+$ cell in the colony, and classified the *smedwi-1*$^+$ cell pairs
150 based on their *smedwi-1* expression levels: high-level pairs indicated symmetric renewal, while pairs with
151 one high and one low *smedwi-1*$^+$ cell categorized as asymmetric division (Fig 2D). By analyzing 40 dividing
152 pairs we estimated that 50% of divisions that produce at least one neoblast are symmetric renewal
153 divisions, in agreement with previous findings (Lei et al., 2016; Raz et al., 2021).

154 The value of *q*, representing symmetric differentiation and neoblast loss probability (Raz et al., 2021), also
155 plays a role in colony dynamics (Fig 2E, S1B). Yet the value of this parameter is more difficult to estimate
156 experimentally (e.g., naïve measurement of cell death using TUNEL in irradiated planarians would be
157 insufficient, because cell death is not limited to neoblasts). We analyzed the effect of different neoblast
158 elimination probabilities on colony size (Fig 2E; Fig S1B-E), and compared the estimates of the analysis
159 with colony size in our experimental data and by extracting colony size measurements from published
160 literature (Fig 2E-F; Methods) (Raz et al., 2021; Wagner et al., 2012, 2011). Considering an average cell
161 cycle length of 29.7 hours, the experimental data indicated that the average colony size was affected by
162 symmetric differentiation or loss probability (*q*), estimated at ~10% of the neoblasts in each cycle (Fig 2E,
163 Fig S1B-E). Given the values derived for *q*, we can conclude that symmetric renewal (*p*) and asymmetrically
164 dividing neoblasts each account for 45% of cell divisions (Fig 2G; Methods).
165
166 *In vivo*, we observed a large variation in the size of the colonies at each time point (Fig 2F). This could be
167 a consequence of an altered delay between irradiation and the onset of colony growth, or from a
168 stochastic decision to undergo symmetrical or asymmetrical division in the early colony. Despite this
169 variability, the observed exponential growth suggested a steady proliferation rate once the colony
170 founding neoblast recovered at day four (Fig 2E, S1A).

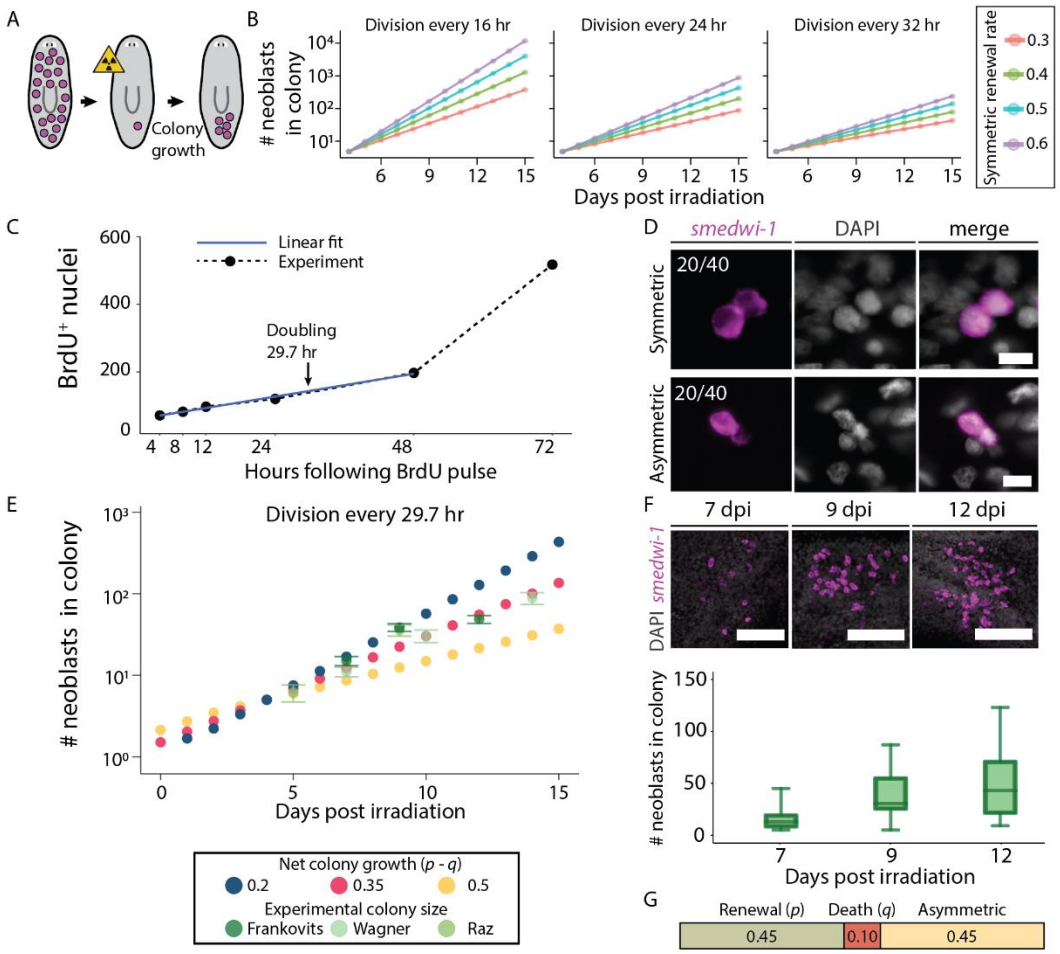

Figure 2. Parameters determining neoblast colony size. (A) Outline of colony growth following subtotal irradiation. Planarians are irradiated to eliminate all neoblasts (purple dots) except for a single survivor. The surviving neoblast forms a proliferating neoblast colony. (B) The impact of average cell cycle length (τ) and probability of symmetric renewal division (*p*) on colony size is shown (*q* was set to 0). (C) Re-analysis of BrdU incorporation time series (Lei et al., 2016) in expanding planarian colonies was used for determining the average cell cycle length (Methods). Linear regression (blue line; y = 59.77 + 2.81 * t; Pearson r = 0.997) was used to identify the doubling time of the colony, and was determined as 29.7 hours (black arrow). (D) The fraction of symmetric renewal divisions was estimated by examining neoblast pairs in colonies (Methods). Scale = 10 µm. (E) The impact of symmetric differentiation or neoblast elimination on colony size was tested, assuming a 29.7 hour long cell cycle. Experimental data of colony sizes at different time points were overlaid to determine the value of biologically relevant parameter. Frankovits data collected here; Wagner, reanalysis (Wagner et al., 2012); Raz, reanalysis (Raz et al., 2021). Error bars show the standard error. (F) Shown are neoblast colonies at three time points following subtotal irradiation. Representative images (z- projection) are shown (top), and neoblast counting of different colonies is shown (box indicates interquartile range; whiskers show range; horizontal bar indicates median). Scale = 100 µm. (G) The estimated fractions of divisions leading to symmetric renewal, symmetric differentiation or elimination, and asymmetric divisions.

186 **Inhibition of lineage differentiation reduces neoblast colony size**

187 Regulating growth and homeostasis requires balancing self-renewal and progeny production. To better
188 understand how neoblasts maintain this balance, we focused on the interplay between the overall growth
189 of the colony and the ability of individual neoblasts to express FSTFs, which are required for specific
190 progeny production (Scimone et al., 2014). More specifically, we investigated how inhibiting
191 differentiation into specific lineages, by suppressing FSTF expression, influences colony size. Considering
192 the linear correlation between post-mitotic progeny production and neoblast number (van Wolfswinkel
193 et al., 2014; Wagner et al., 2012), we hypothesized three potential outcomes (Fig 3A) and their probable
194 effects on symmetric renewal (*p*) and symmetric differentiation or elimination (*q*): (1) Unchanged: *p* and
195 *q* remain balanced, resulting in no change in colony size. This outcome would suggest that the balance of
196 self-renewal and progeny generation is preserved through compensatory production of alternative cell
197 types when differentiation to a specific lineage is suppressed. (2) Larger: An increase in *p*, leading to larger
198 colonies, possibly due to fewer asymmetric divisions in the blocked lineage. (3) Smaller: An increase in *q*,
199 leading to smaller colonies, possibly because neoblasts committed to the blocked lineage have become
200 dysfunctional. We used published frequencies of three major lineages (epidermis, intestine, and *foxF-1*$^{+}$
201 neoblasts) to estimate the size of the colony in each of the described scenarios (Fig 3A) (Raz et al., 2021;
202 Scimone et al., 2018, 2014; van Wolfswinkel et al., 2014). Theoretically, inhibiting a predominant lineage,
203 such as the epidermal lineage (28%), may significantly affect colony size, which could be observed
204 experimentally, whereas changes in colony size following inhibition of smaller lineages could be difficult
205 to distinguish within the experimental time scale.
206
207 On the basis of this assumption, we inhibited differentiation into the epidermal lineage after subtotally
208 irradiating planarians. Following a four-day recovery after subtotal irradiation, we suppressed the FSTF
209 *zfp-1*, which is critical for production of differentiating epidermal progenitors (Fig S2) (Cheng et al., 2018;
210 Tu et al., 2015; van Wolfswinkel et al., 2014; Wagner et al., 2011), but does not impact directly other
211 lineages (van Wolfswinkel et al., 2014). Then, we evaluated neoblast colony sizes in *zfp-1*-suppressed (*zfp-*
212 *1* (RNAi)) planarians at three time points (7, 9, and 12 days post-irradiation; dpi), and compared them with
213 control colony sizes (Fig 3B, Methods). Initially (7 dpi), colony sizes were similar. However, at 9 dpi, *zfp-1*
214 (RNAi) colonies were significantly smaller than in controls. Moreover, unlike in controls, *zfp-1* (RNAi)
215 colonies showed no additional growth, on average, during the period between 9 dpi and 12 dpi, though
216 there was a slight increase in the median colony size (Fig 3B).
217

218 Our basic assumption was that reduction in colony size (vs. control) following *zfp-1* inhibition would
219 indicate an increase in symmetric differentiation or elimination (*q*). However, an alternative possibility is
220 that *zfp-1* inhibition causes mitotic arrest in neoblasts—which would prevent proliferation but would not
221 necessarily result in cell death. We tested whether *zfp-1* (RNAi) colonies had a lower number of cycling
222 neoblasts. We detected neoblasts in mitosis using immunofluorescence (IF) with an anti-H3P-antibody
223 (Fig 3C; Methods). We found that control colonies did not significantly differ from *zfp-1* (RNAi) colonies in
224 the number of $H3P^+$ cells, either in absolute numbers or normalized to average neoblast counts in colonies
225 (Methods). This result suggested that FSTF inhibition did not cause a general mitotic arrest. Further
226 analysis with 2'-Deoxy-2'-fluoro-5-ethynyluridine (EdU) labeling (Fig 3D; Methods) showed a substantial
227 decrease in EdU^+ nuclei in *zfp-1* (RNAi) animals (vs. controls), indicating reduced new cell production.
228 However, normalizing EdU^+ nuclei to average colony size (Fig 3D; Methods) revealed a comparable
229 proportion of cells entering S-phase. Given the unchanged ratios of cycling and mitotic cells, we can
230 conclude that the diminished colony size following *zfp-1* suppression is indeed likely to result either from
231 increased symmetric differentiation or neoblast elimination (*q*). We further suggest that neoblast
232 elimination is a more plausible explanation than increased symmetric differentiation: If *zfp-1* suppression
233 were to lead to increased symmetric differentiation, we would expect to observe a noticeable decline in
234 the number of neoblasts within colonies, while proliferation rates remained stable. Yet, the non-
235 significant difference in EdU-labeling (Fig 3D) between *zfp-1* (RNAi) and control colonies suggested that
236 inhibition of the FSTF *zfp-1* likely led to increased neoblast elimination.

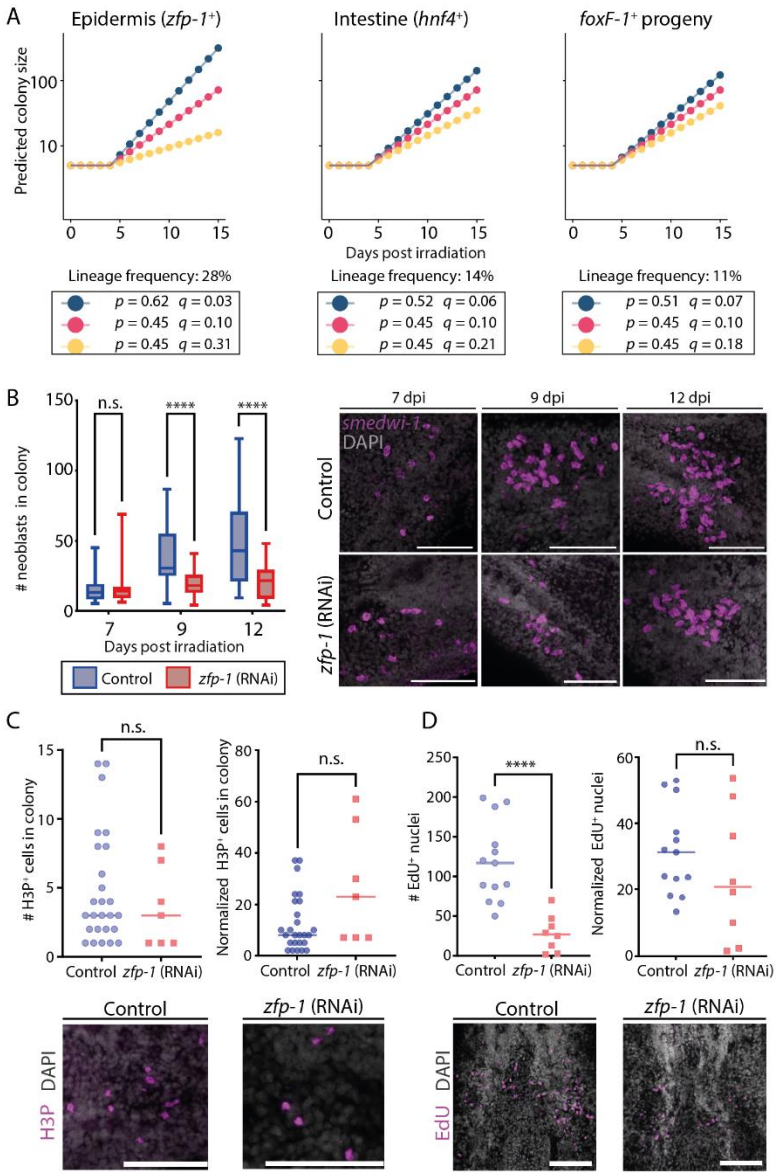

Figure 3. Reduced neoblast colony size following lineage specification block. (A) Models for lineage growth. Potential outcomes of lineage inhibitions were assessed by altering the colony growth and degradation parameters. Applying known lineage frequencies (Raz et al., 2021) to the models indicated that inhibiting production of a major lineage could dramatically impact colony size (left, epidermis). By contrast, inhibition of smaller lineages (middle, right) might have a smaller impact, which would be difficult to detect (Blue: increase in symmetric renewal; red: unchanged renewal and degradation; yellow: increase neoblast degradation). Growth was calculated using the following values: $N_0 = 5$, $\tau = 29.7$ hr, and growth lag time of 5 days (Raz et al., 2021; Wagner et al., 2012). (B) Shown are counts (left) of neoblasts in colonies at three time points following irradiation, which was followed by inhibition of *zfp-1* or control by RNAi. Lineage inhibition resulted in a highly significant decrease in colony size at later time points (box indicates interquartile range (IQR), whiskers show range, bar indicates the median). Number of control colonies analyzed at 7 dpi n = 28; at 9 dpi n = 30; at 12 dpi n = 30; Number of *zfp-1* (RNAi) colonies analyzed at 7 dpi n=15; at 9 dpi n=30; at 12 dpi n = 30. Representative colonies (z-projection) are shown (right). (C) Comparison of absolute (top-left) or normalized (top-right) H3P$^+$ cell number in *zfp-1* (RNAi) and control colonies showed a non-significant

difference (Methods). Representative H3P labeling images are shown (Bottom). Importantly, the number of detectable H3P$^+$ cells was small. (D) Comparison of (top-left) EdU$^+$ nuclei in *zfp-1* (RNAi) and control colonies showed a significant reduction, contributing to the smaller colony size. Comparison of normalized EdU$^+$ nuclei numbers (top-right) showed a non-significant difference, indicating that a similar proportion of neoblasts in the colony were cycling (Methods). Representative EdU labeling images (z-projection) are shown (Bottom). Statistical significance was assessed using Mann-Whitney two-tailed test (Methods). n.s., not significant, ** *P* < 0.0001. Scale = 100 µm.**

Specialized neoblasts are produced in *zfp-1* (RNAi) colonies

Building upon our findings regarding lineage-specific inhibition effects, we next investigated how RNAi of *zfp-1* affected the prevalence of other specialized neoblasts in colonies. We hypothesized that if neoblast elimination was the primary effect of *zfp-1* inhibition, we would observe an absolute decrease in specialized neoblasts of other lineages (e.g., intestine), but not necessarily a relative decrease. We used subtotal irradiation, and following recovery we inhibited *zfp-1*. Then, we counted specialized neoblasts expressing intestine lineage markers (Scimone et al., 2014; Wagner et al., 2011) , and *tgs-1* (Raz et al., 2021; Zeng et al., 2018), which is suggested to label neural progenitors (Fig 4A-B; Methods). Both control and *zfp-1* (RNAi) colonies contained specialized neoblasts. Notably, a decrease in intestine specialized neoblasts was detectable, aligned with the reduced colony size (Fig 4A). Small numbers of *tgs-1*$^+$ neoblasts were observed, with no significant reduction in their counts (Fig 4B). Together, these results suggested that specialized neoblasts were produced in *zfp-1* (RNAi) colonies, but that production of other (non-suppressed) lineages did not increase. This indicated that neoblast elimination predominantly accounts for the reduction in colony size following suppression of the epidermal lineage, without compensation by overproduction of other lineages.

To further analyze the impact of *zfp-1* inhibition on colony growth, we examined the numbers of neoblasts in 64 control colonies and in 53 *zfp-1* (RNAi) colonies, at 12 dpi (Fig 4C-D). The proportion of colonies containing five or more neoblasts was greater in the control group (75%) than in the *zfp-1* (RNAi) group (45%; Fisher's exact test two-tailed *P* = 0.001). Importantly, more *zfp-1* (RNAi) animals failed to develop colonies compared to controls (55% and 25%, *zfp-1* (RNAi) and control colonies, respectively). This might have resulted from the stochastic selection of a *zfp-1* identity by the neoblasts that initially established the colony, and which led to their further dysfunction, and was therefore detrimental to the development of the colony.

Simulation of colony growth following *zfp-1* inhibition

We developed a simulation to recapitulate the observed reduction in colony growth following *zfp*-1 inhibition. Our simulation methodology was designed to mimic real-world neoblast dynamics under *zfp-1* inhibition in a colony, using empirically derived probabilities for each cell cycle outcome. First, we randomly sampled initial colony sizes from the set counted at 7 dpi (Fig 3B). In every simulation cycle, each neoblast fate was selected based on the probabilities of cell cycle outcomes identified above, derived from empirical data (symmetric renewal, asymmetric division, symmetric differentiation or elimination; Fig 2G). The change in colony size was calculated over approximately six cell cycles. We conducted 100 iterations per simulation and compared the results with experimental data (Fig 4E; Methods). The simulated colony sizes closely matched the experimental observations. When simulating *zfp-1* (RNAi) colony growth by increasing the symmetric differentiation or elimination probability (q) by the known proportion of *zfp-1*$^+$ neoblasts, the model recapitulated the experimental findings (Fig 4E-F). Notably, many simulated *zfp-1* (RNAi) colonies failed to grow, often because of initial sampling of a state of symmetric differentiation or elimination, prohibiting further development of the colony (Fig 4F).

The agreement of these simulations with the experimental results is aligned with a model where neoblasts independently select their cell cycle outcome based on a replication outcome distribution without maintaining any memory of previous replication outcomes. Moreover, inhibition of a gene required for neoblast differentiation (e.g., FSTF) impedes the contribution of neoblasts that randomly selected this identity from any further contribution to colony growth across the timescale of the simulation.

Combined suppression of low-frequency lineages affects neoblast colony formation

Our model and simulations indicate that inhibition of smaller lineages will not result in detectably smaller colonies (Fig S3A-C). We tested this model prediction by comparing colonies produced following suppression of intestine lineage progenitors (Forsthoefel et al., 2012; van Wolfswinkel et al., 2014; Wagner et al., 2011), which account for 14% of the produced progenitors (Raz et al., 2021). Indeed, highly efficient inhibition of the intestine lineage by RNAi (Fig S3D), did not result in reduced colony size or colony production, in agreement with our model (Fig 4G-H, S3A). This result corroborated the model's predictions regarding lower-frequency lineages (Fig 3A): the potential increase in q following suppression of differentiation to a lower-frequency lineage had undetectable effect on colony size. However, the model predicts that inhibition of several lineages, which collectively amount to a larger fraction of produced

progenitors, may generate a detectable difference in successful colony establishment. We co-suppressed the production of intestine lineage together with *foxF-1*$^{+}$ progenitors, which together amount to 25% of the progenitors (Raz et al., 2021), following subtotal irradiation (Fig 4I). The co-inhibition of the two lineages resulted in a highly significant increase in the failure to establish colonies (8/9; 88.9%), compared to their controls (3/19; 15.8%; Fisher's exact test two-tailed P = 4×10^{-4}).

These results reinforce the hypothesis that FSTF inhibition reduces colony growth (vs. control), primarily through increased neoblast elimination, without compensatory increases in other lineages. The results also suggest that a neoblast that has selected an identity, but that cannot complete proliferation and differentiation, will not be able to adopt any other identity in this experimental timescale. Based on these conclusions, we propose a semi-stochastic model for selecting the outcome of neoblast division, assuming no memory or coordination between cells, that is sufficient for describing neoblast colony growth.

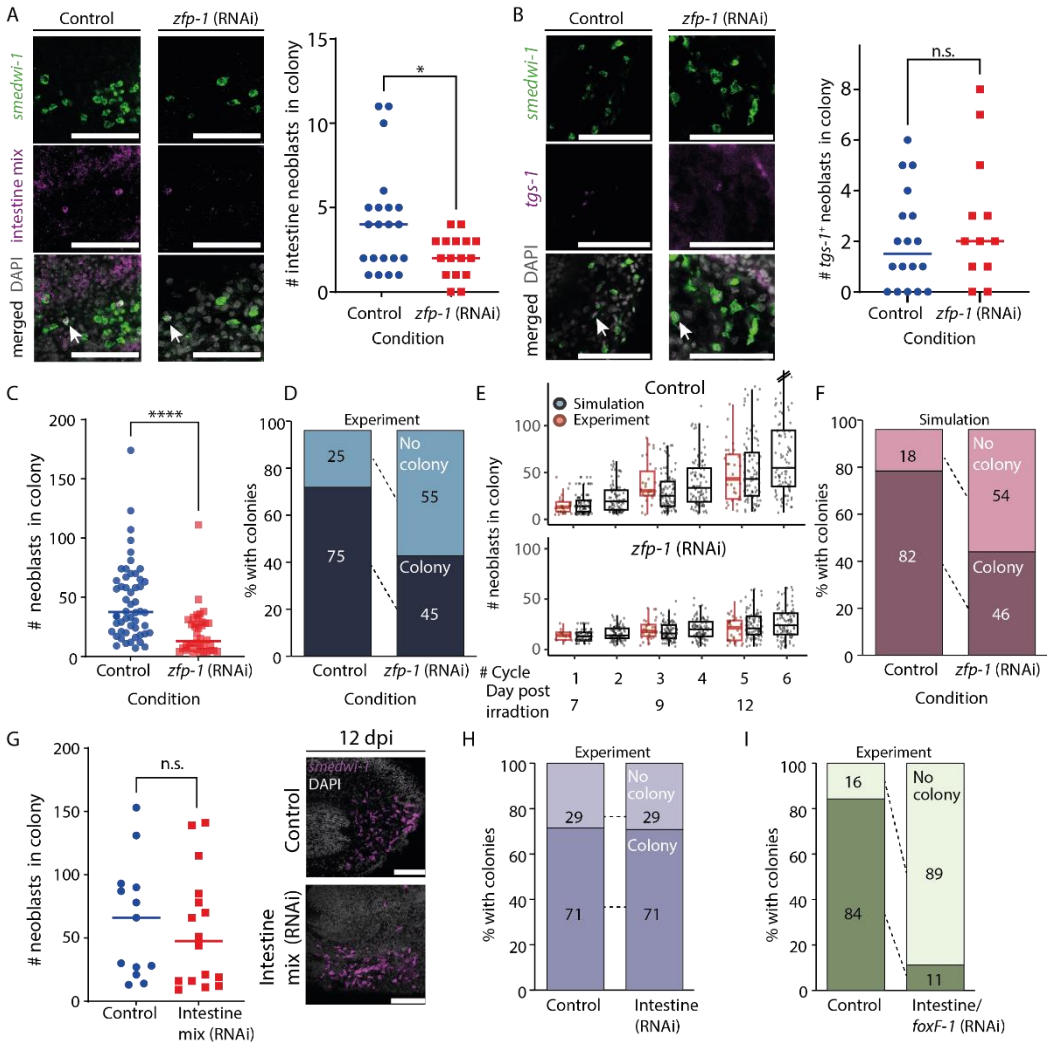

Figure 4. Simulation of neoblast colony growth following lineage block. (A-B) Neoblasts expressing lineage gene expression markers were detected using FISH (intestine mix: *hnf-4, gata4/5/6,* and *nkx2.2*; *tgs-1*), and were counted in colonies of control and *zfp-1* (RNAi) animals at 12 dpi (Methods). Left panels show confocal images of representative colonies (Methods); quantification of the experiment is shown on the right. Scale= 100 µm. (C) Comparison of colony size in control and in *zfp-1* (RNAi) animals 12 dpi showed a highly significant reduction in the size of *zfp-1* (RNAi) colonies (Mann-Whitney two-tailed test, **** $P < 0.0001$). Data is also shown in Fig 3B. (D) Summary of colony production in control and *zfp-1* (RNAi) animals based on analysis of 64 and 53 control and *zfp-1* (RNAi) colonies, respectively, at 12 dpi. Developed: ≥ 5 neoblasts detected; No colony < 5 neoblasts detected. (E) Simulation of colony growth in control and *zfp-1* (RNAi) animals, bottom and top, respectively (Methods). Shown are multiple iterations (black dots; n = 100 for each condition) of colony size simulation starting at 7 dpi. Experimental data quantifying colony sizes are shown (red dots) next to the corresponding simulation cycle. Box indicates the IQR; whiskers indicate ±1.5 x IQR; values out of the whisker range (outliers) were removed for clarity. (F) Summary of colony production in simulated control and *zfp-1* (RNAi) animals based on experimentally determined lineage frequencies, and assuming no memory in division outcome decision. Developed colony: ≥ 5 neoblasts in the simulation on day 12. (G) Neoblasts were counted in colonies 12 dpi, which was followed by inhibition of intestine progenitors by combined RNAi treatment (*hnf-4*, *gata4/5/6*, *nkx2.2*). Lineage inhibition did not affect colony size (left). Representative colonies (z-projection) are shown (right). Scale = 100 µm. (H-I) Summary of colony establishment in control and RNAi animals. (H) Suppression of intestine lineage did not affect the likelihood of producing colonies (n = 21 and 24, control and RNAi animals, respectively). (I) Combined suppression of *foxF-1* (Scimone et al., 2018) and intestine lineage production resulted in a significant reduction in the likelihood of producing colonies (Fisher's exact test two tailed $P = 4x10^{-4}$; n = 19 and 9, control and RNAi animals, respectively).

Inhibition of *zfp-1* does not induce overexpression of other lineages in homeostasis

Clonal analysis is a powerful approach for studying neoblast proliferation and progeny production. However, stem cell behavior in homeostasis may differ from that observed in clonal growth. For example, unlike in clonal expansion, the stem cell population size remains unchanged during homeostasis, indicating the differential activity of feedback mechanisms. Moreover, the vastness of the neoblast population in homeostasis allows to examine the ability of neoblasts to respecify their lineage overtime, and to determine if FSTF inhibition results in an increase to cell loss rate.

We examined whether the suppression of a major lineage production has resulted in overproduction of other lineages, a phenomenon that we did not observe in colonies. First, we used two published gene expression datasets from FACS-purified S/G2/M neoblasts in *zfp-1* (RNAi) and control animals collected at various time points (Cheng et al., 2018; van Wolfswinkel et al., 2014) (Methods). We utilized pre-calculated tables of differentially expressed genes in these datasets (Hoffman and Wurtzel, 2023), and annotated the cell types that express them (Fincher et al., 2018). Most downregulated genes with known neoblast lineage enrichment (Fincher et al., 2018) were epidermal (82%, 55/67; Fig 5A; Table S1;

354 Methods). Conversely, upregulated genes following *zfp-1* suppression were primarily associated with
355 protonephridial or neural neoblasts (30/57 and 20/57 genes, respectively; Fig 5B; Table S2), consistent
356 with the original data analysis (Cheng et al., 2018). Notable upregulated genes included transcription
357 factors, such as *nkx2-like* (Currie et al., 2016), *hunchback-like* (Reddien et al., 2005a), *runt-1* (Sandmann
358 et al., 2011; Wenemoser et al., 2012), and *tgs-1* (Zeng et al., 2018). Overexpression was evident from an
359 intermediate timepoint (9 days post RNAi), whereas epidermal genes downregulation occurred earlier (6
360 days post RNAi; 30%, 20/67; FDR < 1E-5).
361
362 We hypothesized that biologically meaningful upregulation of neuron- and protonephridia-associated
363 genes in neoblasts following *zfp-1* inhibition would result in overexpression of genes associated with these
364 cell types in whole tissues, reflecting their increased production. To test this hypothesis, we examined
365 published gene expression data from whole and regenerated tissues following *zfp-1* inhibition (van
366 Wolfswinkel et al., 2014; Zeng et al., 2018). Predictably, the majority of downregulated genes were
367 associated with the epidermis (70%, 490/698; Fold change < -2; FDR < 1E-5; Table S3; Methods).
368 Examination of upregulated genes showed that only a small fraction of the genes was associated with
369 either protonephridial (4.9%) or neural (12.7%) expression at any examined time point (Fig 5C; Table S4;
370 Methods). Therefore, gene expression analysis of whole tissues provided no evidence of an
371 overrepresentation of neural or protonephridia cells in *zfp-1* (RNAi) animals, suggesting that cells related
372 to these lineages were not excessively produced. Conversely, 37% of the overexpressed genes following
373 *zfp-1* (RNAi) in the whole tissue libraries were associated with intestinal cell types, despite no evidence
374 for overrepresentation of intestine-associated FSTFs in neoblasts isolated from *zfp-1* (RNAi) animals
375 compared to controls (Table S4).
376
377 In *zfp-1* (RNAi) neoblast colonies, we observed an absolute reduction in cycling cells (Fig 3D). We tested
378 whether this phenotype was recapitulated in homeostatic, unirradiated, *zfp-1* (RNAi) animals by EdU
379 labeling. We injected *zfp-1* or control double-stranded (dsRNA; Methods), and following three and five
380 days, we performed EdU labeling by a 16 hour EdU pulse (Methods). Interestingly, there was an increase
381 in EdU^+ nuclei in the *zfp-1* (RNAi) animals at both timepoints (Fig 5D). Investigating the potential
382 correlation with apoptosis via TUNEL labeling revealed no early increase in cell death, only appearing at
383 later stages (Fig 5E; Methods). Therefore, *zfp-1* inhibition does not trigger an acute rise in neoblast cell
384 death that might induce hyperproliferation.
385

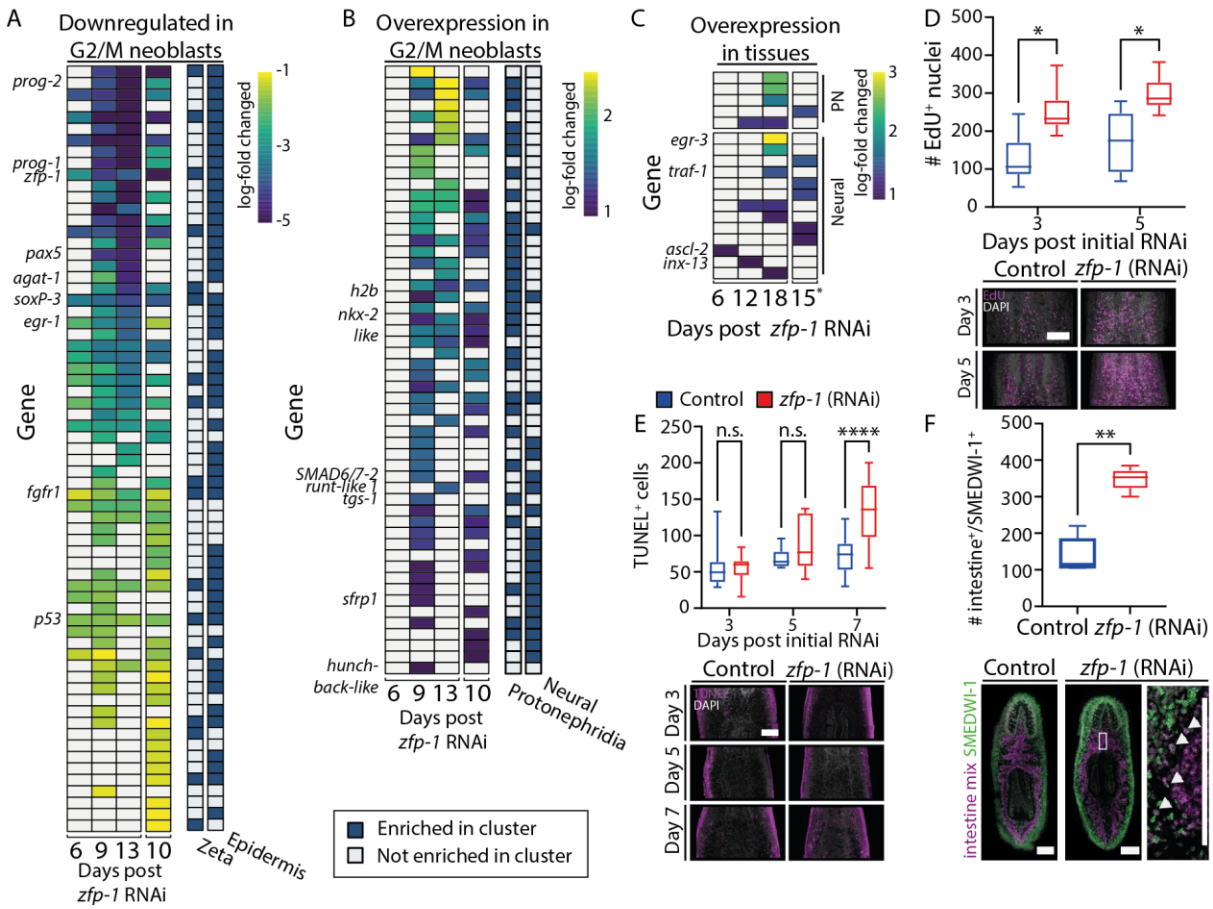

Figure 5. Analysis of *zfp-1* inhibition consequences in homeostasis. (A) Downregulated genes in FACS-purified S/G2/M neoblasts were overwhelmingly associated with expression in the epidermal lineage and epidermis-specialized (zeta) neoblasts (Cheng et al., 2018; Fincher et al., 2018; van Wolfswinkel et al., 2014). (B) Upregulated genes in FACS-purified S/G2/M neoblasts were largely associated with neuronal and protonephridial specialized gene expression (Fincher et al., 2018). (C) Analysis of overexpressed genes of whole-tissues following *zfp-1* inhibition showed that only a few factors were associated with protonephridia or neurons. (A-C) Heatmaps showing row-scaled gene expression obtained from PLANAtools (Hoffman and Wurtzel, 2023) Blue and yellow, low and high log-fold gene expression difference, respectively. Columns on the right indicate cell type-specific gene expression (Fincher et al., 2018). (D) Counting EdU⁺ nuclei in unirradiated control and *zfp-1* (RNAi) animals. (E) Counting apoptotic cells in unirradiated control and *zfp-1* (RNAi) animals (Methods). (F) Counting intestinal progenitors showed an increase in progenitors at later time points, in agreement with the gene expression analysis of *zfp-1* (RNAi) of whole tissues. Scale = 100 µm. * *P* < 0.05; ** *P* < 0.01; ** *P* < 0.0001.**

Colony sizes following *zfp-1* (RNAi) were reduced, yet cycling cell numbers in homeostasis were increased. Similar results were reported for the epidermal regulator *Smed-p53* (Cheng et al., 2018; Pearson and Sánchez Alvarado, 2010): neoblast colonies following *p53* (RNAi) are strikingly smaller (Wagner et al., 2012), yet in homeostasis, *p53* (RNAi) animals show an increased number of mitoses (Pearson and

403 Sánchez Alvarado, 2010), and even initially an increase in canonical neoblast markers (Pearson and
404 Sánchez Alvarado, 2010).
405 Considering that in homeostasis *zfp-1* (RNAi) planarians show greater numbers of cycling cells (Fig 5D) and
406 intestinal gene overexpression in tissue (Table S4) as compared with controls, we conducted a targeted
407 analysis to quantify the number of newly generated intestine progenitors in *zfp-1* (RNAi) animals. We
408 counted intestine progenitors *in situ* (Fig 5F; Methods), and found a higher proportion of intestine
409 progenitors in the *zfp-1* (RNAi) animals as compared with controls (Fig 5F; Mann–Whitney two-tailed U
410 test $P = 0.008$). Interestingly, in our analyses of growing colonies, we did not observe a parallel difference
411 in intestine neoblast proportion (Fig 4A), leading us to speculate that the rise in cycling cells in homeostasis
412 was an indirect effect of *zfp-1* RNAi suppression, and indicating of the limits of neoblast analysis in
413 colonies. In other words, integration of the analysis from homeostasis with our colony data suggests that
414 *zfp-1* inhibition did not lead to a direct amplification of other lineages, but more likely to an indirect
415 amplification of the intestine lineage.

416 **Discussion**

417 Understanding how stem cell proliferation and lineage choices are regulated is critical for elucidating
418 mechanisms of growth and homeostasis (Chan et al., 2021; Dagan et al., 2022; Ferraro et al., 2010; Lei et
419 al., 2016; Li and Xie, 2005; Morrison and Spradling, 2008; Scimone et al., 2010; Zhu et al., 2015).
420 Neoblasts form a simple yet powerful system, which has features of both adult stem cells and their transit-
421 amplifying cell progeny (Adler and Sánchez Alvarado, 2015; Baguñà, 2012; Reddien, 2018). Functionally,
422 neoblasts can repopulate stem cell-depleted planarians, produce a diversity of cell types, and adjust their
423 growth rate according to organism requirements and nutrient availability (Hayashi et al., 2006; Salvetti et
424 al., 2009; Steele and Lange, 1976; Wang et al., 2018). Herein, we sought to test whether growth in a
425 neoblast colony is consistent with a model that does not assume communication between neoblasts or

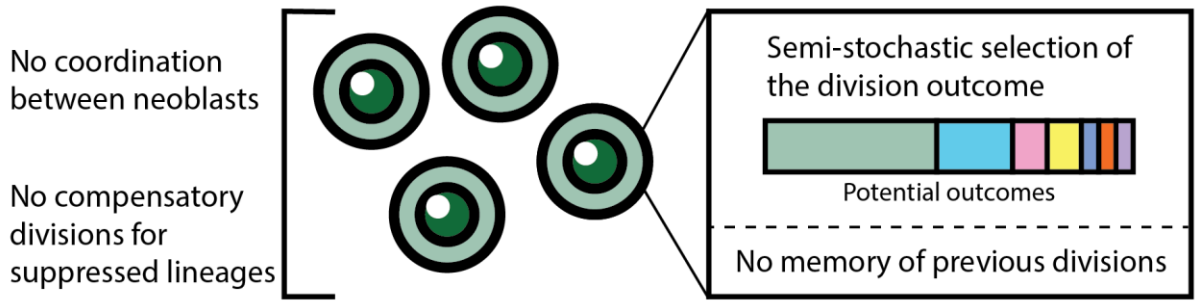

Figure 6. Model summarizing neoblast colony growth principles.

426 memory of cell fate decisions, but instead relies on stochastic selection of division outcome (Fig 6). We
427 further sought to enrich this model by understanding the interplay between neoblast lineage decisions
428 and colony growth.

429 **Analysis of neoblast colony expansion**

430 The initial model we developed was grounded in simple principles of colony growth (Eq 1, Fig 2B), in which
431 cell fate decisions are made stochastically and independently of one another, as a function of the following
432 parameters: average cell cycle length, symmetric renewal rate, and symmetric differentiation and
433 neoblast elimination rate. We experimentally derived parameter values and compared the model's
434 predictions to experimental data. Our findings suggested that the reliance on minimal assumptions
435 provides a good description of neoblast colony growth following subtotal irradiation. The model captured
436 the average colony growth within the tested time range, despite notable variability in observed colony
437 sizes at a given time point. Based on these results, we suggest that if slow cycling neoblasts (Molinaro et
438 al., 2021) emerge in colonies, their contribution for colony growth is likely negligible, allowing their
439 exclusion from the model without sacrificing accuracy.
440
441 To better understand the potential consequences of random neoblast loss or excessive symmetric
442 differentiation at early stages of colony growth, we used colony growth simulations, where each cell
443 selected independently the outcome of its division. These simulations predicted that a fraction of colonies
444 would fail to develop because of these random effects, a prediction that was corroborated by
445 experimental results. This alignment demonstrates the utility of neoblasts as a system for studying stem
446 cell colony formation and exploring concepts of stem cell behavior.

447 **Consequences of lineage-specific differentiation inhibition**

448 Moving from the fundamental aspects of neoblast colony growth, we next tested how limiting lineage
449 identity selection affected neoblasts. We suppressed the expression of key fate-specifying genes to dissect
450 how stem cells respond to inhibition of their differentiation trajectory. The transition from measuring
451 general colony growth to specific lineage perturbations allowed us to examine the association of
452 proliferation and lineage specification. In particular, suppressing the master epidermal regulator *zfp-1*,
453 corresponding to the most abundant planarian cell lineage (Cheng et al., 2018; Raz et al., 2021; van
454 Wolfswinkel et al., 2014), drastically reduced neoblast colony growth. This observation led us to consider

455 how stem cells in a colony balance self-renewal and differentiation, and why both processes were
456 disrupted by blocking differentiation to a single lineage. We suggest several interpretations for this
457 observation: First, if we assume that a neoblast can alternate between self-renewal and production of
458 differentiated progeny in each cell cycle, then a decision to produce a blocked progeny may preclude
459 further divisions of the neoblast. A second possibility is that the presence of a specific lineage, epidermal
460 progenitors in this case, is required for other neoblasts to proliferate; in this case, suppression of
461 differentiation could indirectly limit colony growth. The first interpretation is more likely relevant for
462 understanding colony growth given our observation that combined suppression of several smaller
463 lineages produced a similar inhibition to colony establishment.

464 The progressive reduction in colony size indicated that inhibition of a specific lineage reduced the fraction
465 of neoblasts that contributed to colony growth, possibly due to their failure to produce the blocked
466 lineage and to alter their progeny identity. Interestingly, in unirradiated animals with abundant neoblasts,
467 *zfp-1* inhibition led to increased cell proliferation – a response also noted after suppressing other
468 regulatory genes like *Smed-p53* (Pearson and Sánchez Alvarado, 2010). This proliferation increase
469 appeared before a rise in cell death, suggesting that cell death did not induce excessive proliferation in
470 early stages. The difference in the consequence of lineage suppression in a neoblast colony and in
471 unirradiated animals indicates that differential activity of feedback mechanisms regulates neoblast
472 proliferation. We speculate that following subtotal irradiation, the near complete depletion of neoblasts
473 and their progeny (Eisenhoffer et al., 2008), alters the regulation of surviving neoblasts, and leading to
474 their rapid proliferation, which is not typical for neoblasts in homeostasis (Wenemoser and Reddien,
475 2010). Further investigation is needed into compensatory mechanisms that planarians use to maintain
476 overall tissue integrity when differentiation processes are disrupted.

477 **A stochastic model for independent selection of cell division outcome in colonies**

478 Our study investigates the mechanism behind neoblast division outcome selection. An exponential growth
479 function describes the increase in colony size and the differentiation of progeny in the timescale of the
480 analysis, closely aligning with our experimental results and published data (Raz et al., 2021; Wagner et al.,
481 2012). Notably, this function operates without parameters for coordination of division outcome between
482 neoblasts, or neoblast memory. It posits that division outcomes are guided by an innate distribution of
483 cell fates encoded within the neoblasts. We hypothesize that this distribution is modifiable by regional
484 signals (e.g., Wnt, BMP), which indicate the neoblast location (Gaviño and Reddien, 2011; Petersen and

485 Reddien, 2008; Wurtzel et al., 2017), and by injury signals (e.g., ERK), that modulate division rate (Bohr et
486 al., 2021; Fan et al., 2023; Tasaki et al., 2011; Wurtzel et al., 2015). This strategy facilitates the dynamic
487 balance in cell lineage production and meeting the organism needs without direct communication
488 between neoblasts, and promotes return to homeostasis.
489
490 The emerging model enhances the understanding of neoblast dynamics and contributes to broader
491 knowledge of stem cell behavior. The interplay between lineage-specific differentiation, proliferation, and
492 resultant physiological adaptations presents a robust strategy for using pluripotent stem cells for re-
493 achieving balance, in a manner that is not found in many non-regenerative organisms. This could inspire
494 future research of pluripotent stem cells and their applications for regenerative biology.
495

496 # Methods

497 ## Gene cloning and transformation

498 Selected genes were amplified using planarian cDNA and gene-specific primers, and cloned into pGEM-T
499 Easy vector using pGEM-T Easy Vector System I (Promega; CAT A1360). Vectors were transformed into
500 *Escherichia coli* using the heat-shock method. Briefly, 5 µl of cloned plasmid were mixed with 100 µl of *E.*
501 *coli* TOP10 bacteria and incubated on ice for 30 min. Next, bacteria were incubated for 45 s at 42°C, moved
502 immediately to ice, and recovered in 350 µl of Luria Broth (LB) medium for 1 h at 37°C. Then, 100 µl of
503 recovered bacteria were plated on agarose plates containing 1:1,000 Ampicillin, 1:200 Isopropyl β- d-1-
504 thiogalactopyranoside (IPTG) and 1:625 5-bromo-4-chloro-3-indolyl-b-D-galactopyranoside (X-Gal). Plates
505 were incubated overnight at 37°C, and colonies were screened by colony PCR using M13F and M13R
506 primers with the following PCR program: (i) 5 min at 95°C; (ii) 34 cycles of 45 s at 95°C, 60 s at 55°C, and 2
507 min at 72°C; (iii) 7 min at 72°C; (iv) hold at 10°C. Reactions were analyzed by gel electrophoresis, and
508 colonies having the correct fragment were grown overnight in LB medium, supplemented with 1:1,000
509 Ampicillin at 37°C in 180 rpm. Plasmids were purified with the NucleoSpin Plasmid MiniprepKit (CAT
510 740588, Macherey-Nagel) and sequenced by Sanger sequencing. Primer sequences used for cloning the
511 following genes: *hnf-4*, forward primer GATCTCGCACAATGCACTCG, reverse primer
512 GTCTCACGAACTCCTTGCCA; *nkx2.2*, forward primer TTTGGTGCCAGCAGACTCAA, reverse primer
513 TAGAGCCAGCTAATGTGGCG; *gata4/5/6*, forward primer CGGTATTGTCGAATTCTCACCAG, reverse primer
514 TGACATCGCAATTGGAACCG; *foxF-1*, forward primer GTCCTATTTCCAGCACACAGC, reverse primer
515 TCCGGAATCGTGCTGAGG.

516 ## Near complete neoblast ablation by subtotal irradiation

517 Animals were irradiated using a BIOBEAM GM 8000 (Gamma-Service Medical GmbH). To generate 1-3
518 colonies per animal, 2 mm starved (> 7 d) worms were irradiated with 1750 rads (Wagner et al., 2012).
519 Worms were allowed to recover and washed in planarian water a day after the irradiation.

520 ## Synthesis of dsRNA for feedings and microinjections

521 DsRNA was synthesized as previously described (Rouhana et al., 2013). Briefly, templates for in vitro
522 transcription (IVT) were prepared by PCR amplification of cloned target genes using forward and reverse
523 primers with flanking T7 promoter sequences on the 5' end. dsRNA was synthesized using the
524 TranscriptAid T7 High Yield Transcription Kit (CAT K0441, Thermo Scientific). Reactions were incubated

525 overnight at 37°C and then supplemented with RNase-free DNase for 30 min. RNA was purified by ethanol
526 precipitation and resuspended in 70 µl of ultra-pure H2O. RNA was analyzed on 1% agarose gel and
527 quantified by Qubit (CAT Q33223, Thermo Scientific) for validating a concentration higher than 5 µg/µl.
528 Animals were starved for at least 7 d prior to RNAi experiments. In clonal expansion experiments, animals
529 were fed with 14 µl of dsRNA mixed with 25 µl of beef liver 4 days post-irradiation. In homeostasis
530 experiments, worms were injected 4 times with dsRNA every other day.

531 **Injections of dsRNA into planarians**

532 Animals were injected with *zfp-1* dsRNA using Nanoject III (CAT 3-000-207, Drummond Scientific
533 company). Briefly, planarians were placed on a cold wet filter paper on their dorsal side, and were injected
534 posterior to the pharyngeal cavity. After the initial puncture, 3 consecutive dsRNA injections of 33 nl each
535 were delivered at a rate of 66 nl/sec. Worms were injected 4 times, every other day, and fixed at different
536 time points for whole-mount analysis.

537 **Planarian fixation for whole-mount assays**

538 Fixation was performed as previously described (King and Newmark, 2013). Animals were killed with 5%
539 N-Acetyl-L-Cysteine (NAC, CAT 1124220100, Mercury) in PBS for 5 min, then incubated with 4%
540 Formaldehyde (FA) in 0.3% PBSTx (Phosphate Buffered Saline, 0.3% Triton X-100) for 20 min. Animals were
541 then washed in PBSTx, 50:50 PBSTx:methanol and stored in methanol at -20°C.

542 **Fluorescence in situ hybridization using tyramide signal amplification**

543 Fluorescence in situ hybridization (FISH) was performed as previously described (King and Newmark,
544 2013) with minor changes. Briefly, fixed animals were bleached and treated with proteinase K (2 µg/ml,
545 CAT 25530-049; Invitrogen) in PBSTx (Phosphate Buffered Saline, 0.3% Triton X-100). Samples were
546 incubated for 2 hr in a pre-hybridization buffer (pre-hyb) followed by an overnight incubation with probes.
547 Samples were washed twice for 30 min in each solution: pre-hyb solution, 1:1 pre-hyb:2×SSCx, 2×SSCx,
548 0.2×SSCx, PBSTx. Blocking was performed in 0.5% Roche Western Blocking Reagent (CAT 11921673001;
549 Sigma-Aldrich) and 5% heat-inactivated horse serum (CAT 04-124-1A; Biological Industries) in TNTx
550 (100 mM Tris pH 7.5, 150 mM NaCl, 0.3% Triton X-100) for 2 hr. Animals were incubated with an anti-DIG-
551 POD antibody (1:1,500; Roche) or anti-DNP-HRP (1:10,000; Perkin-Elmer) overnight at 4°C. After antibody
552 washes, tyramide development was performed as previously described (King and Newmark, 2018).
553 Following development, peroxidase activation was quenched in a 1% sodium azide solution for 1 hr,

554 followed by 6 PBSTx washes and antibody labeling for the second probe. Samples were labeled with DAPI
555 (1:5000 in PBSTx) overnight at 4°C and mounted with Vectashield (CAT H-1000-10; Vector Laboratories).

556 **Immunofluorescence combined with FISH**

557 Animals were fixed with 5% NAC, bleached, and treated with proteinase K as described for FISH analysis.
558 Samples were incubated for 2 hr in pre-hyb followed by overnight incubation with the probes. Samples
559 were washed twice in each solution, for 30 min each: pre-hyb solution, 1:1 pre-hyb:2×SSCx, 2×SSCx,
560 0.2×SSCx, PBSTx. Subsequently, blocking was performed in PBSTB (PBSTx, 0.25% BSA) for 2 hr at room
561 temperature. Animals were then incubated with anti-SMEDWI-1 antibody (a gift from Peter W. Reddien,
562 1:1000) at 4°C overnight. Then, 7 PBSTx washes were performed, followed by incubation with PBSTB
563 blocking solution for 2 hr at room temperature followed by incubation with secondary antibody (goat anti
564 rabbit-HRP, 1:300 in PBSTB) overnight at 4°C. Post-antibody washes and tyramide development
565 (fluorescein tyramide; 1:2000) were performed as previously described (King and Newmark, 2013). After
566 development, peroxidase activity was quenched using 1% sodium azide for 1 hr, followed by 6 PBSTx
567 washes and incubation with anti-DIG antibody (1:1,500; CAT 11207733910; Sigma-Aldrich) overnight at
568 4°C. Post-antibody washes and development with rhodamine tyramide (1:1000) were performed as
569 described above. Samples were incubated with DAPI (1:5000 in PBSTx) overnight and mounted with
570 Vectashield.
571

572 **FISH by hybridization chain reaction**

573 Probe sets (30 pairs per gene) were designed and synthesized by the manufacturer (Molecular
574 Instruments, Los Angeles, CA, USA) for the following genes: *tgs-1* and *smedwi-1*. Worms were fixed and
575 bleached as previously described for FISH. Next, hybridization chain reaction (HCR) was performed
576 according to the manufacturer's HCR RNA-FISH protocol for samples in solution (Choi et al., 2018). DAPI
577 was added during the amplifier's wash steps, for a total incubation time of 2 hr at room temperature.
578 Samples were mounted with Vectashield and stored at 4°C for subsequent analysis.

579 **Metabolic labeling by F-ara-EdU**

580 F-ara-EdU (CAT T511293; Sigma-Aldrich) was first diluted in DMSO to the concentration of 200 mg/ml.
581 Animals were soaked with 2.5 mg/ml F-ara-EdU diluted in planarian water for 16 hr, 24 hr after the
582 indicated injections. For clonal expansion analysis, samples were soaked with EdU for 16 hr at day 11 post

583 irradiation. Samples were fixed, bleached, and treated with proteinase K as described for FISH (King and
584 Newmark, 2013). Next, 3 washes in 3% PBSB (PBS supplemented with 3% BSA) were performed followed
585 by a click reaction using baseclick kit (CAT Back-edu488, baseclick GmbH). Samples were washed 3 times
586 with PBSB, incubated with DAPI (1:5,000 in PBSTx) overnight at 4°C and mounted with Vectashield.

587 **Immunofluorescence labeling by anti-H3P labeling**

588 H3P labeling was performed as previously described (LoCascio et al., 2017; Wenemoser and Reddien,
589 2010) with minor modifications. Briefly, following fixation with 5% NAC, bleaching and proteinase K
590 treatment, blocking was performed with 10% heat inactivated horse serum for 2 hr. Next, anti-phospho-
591 Histone H3 Antibody (CAT 04817; Sigma-Aldrich) was added in the concentration of 1:100 overnight in
592 4°C, followed by 7 PBSTx washes. Samples were incubated in blocking solution for 2 hr and then incubated
593 with goat anti-rabbit-HRP secondary antibody (Abcam; ab6721; 1:300) overnight at 4°C. Samples were
594 washed 7 times with PBSTx, developed using rhodamine tyramide diluted 1:1,000 in PBSTi (PBSTx, 0.07%
595 imidazole), labeled with DAPI overnight at 4°C, and mounted with Vectashield.

596 **Image acquisition and cell counting**

597 Images of samples labeled by FISH, HCR, immunofluorescence, F-ara-EdU and TUNEL were collected using
598 a Zeiss LSM800 confocal microscope. Labeled cells were counted manually using the cell counter module
599 in the ImageJ software (Rueden et al., 2017). Normalization of EdU^+ nuclei was performed by dividing the
600 number of EdU^+ nuclei by the average number of *smedwi-1*$^+$ cells detected in a colony at the corresponding
601 time point, and divided by 10 for readability.

602 **TUNEL labeling**

603 TUNEL was performed as previously described (Pellettieri, 2010) with minor modifications. Briefly,
604 animals were fixed with 5% NAC and bleached overnight with 6% hydrogen peroxide in PBSTx. Animals
605 were then treated with 2 µg/ml proteinase K for 10 min, 4% FA for 10 min, and were then washed twice
606 with PBS. Using ApopTag Red In Situ Apoptosis Detection Kit (CAT S7165; Sigma-Aldrich), 5 animals per
607 tube were incubated with TdT enzyme mix for 4 hr at 37°C, followed by 4 PBSTx washes. Samples were
608 incubated in a blocking solution (0.5% Roche Western Blocking Reagent and 5% inactivated horse serum
609 in TNTx) for 2 hr followed by incubation with anti-DIG antibody (1:1000) overnight at 4°C. Samples were
610 washed 7 times with PBSTx, developed using rhodamine tyramide diluted 1:1,000, labeled with DAPI
611 (1:5000 in PBSTx) overnight at 4°C and mounted with Vectashield.

612 **Estimation of the fraction of symmetric renewal divisions**

613 Estimation of the fraction of symmetric renewal divisions was performed as previously described (Lei et
614 al., 2016; Raz et al., 2021). Colonies from 7, 9, and 12 dpi were labeled by FISH with the pan-neoblast
615 marker *smedwi-1.* Colonies were closely examined using a confocal microscope (Zeiss LSM800) to find two
616 adjacent *smedwi-1*+ cells. Two labeled cells with high expression of *smedwi-1* marker were classified as
617 symmetric division. Pairs composed of high *smedwi-1*+ cell and low *smedwi-1*+ cell were classified as
618 asymmetrically dividing.

619 **Data extraction from published literature**

620 Data was extracted using WebPlotDigitizer by labeling data points (Drevon et al., 2017). Table S5
621 summarizes the extracted data and the original data source.

622 **Estimation of values of colony growth parameters**

623 Counts of neoblast in colonies at different time points following subtotal irradiation (Fig 2F, Table S5) were
624 collected. Curve fitting using an exponential function (Eq 2) was performed with the curve_fit function
625 from the scipy.optimize Python module using the average cell cycle length (τ) extracted from the $BrdU^+$
626 labeling assay (Fig 2C; S1B-E) (Lei et al., 2016). The values of symmetric renewal (p) and symmetric
627 differentiation or elimination (q) were estimated by fitting a range of values for $p - q$ between 0.1 and 0.4
628 and calculating the R-squared values of the fit to the data (S1D-E). Experimental assessment of symmetric
629 renewal (p) and asymmetric division (a) determined that they are equal (i.e., $p = a$; Fig 2D). The best fit,
630 as estimated by examining the sum square of residuals (Fig S1B-E), for $p - q$ was found to be 0.3445. Since
631 (1) all possible division outcomes are $p + q + a = 1$; (2) $p = a$; and (3) $p - q = 0.3445$, we estimated that $p =$
632 0.45 and $q = 0.1$.

633 **Simulation of colony growth**

634 Simulations were performed using custom R code, executing as follows: selection of parameters occurred
635 using selected frequencies of symmetric renewal, and symmetric differentiation or elimination. Initial
636 colony size was determined by randomly selecting a value from empirical distribution of early colony size,
637 as reported in the literature (Raz et al., 2021; Wagner et al., 2011). In each simulation round, every cell
638 underwent selection of an outcome, adhering to the predefined frequencies. This simulation process
639 extended 5 – 20 cycles and was replicated 100 times.

640 **Gene expression analysis of S/G2/M neoblasts**

641 Processed differential gene expression data profiling FACS-purified S/G2/M neoblasts isolated from
642 control and *zfp-1* (RNAi) animals was downloaded from PLANATools (Hoffman and Wurtzel, 2023). Each
643 gene in the table was assigned a cell type identity based on the planarian cell type gene expression atlas
644 (Fincher et al., 2018).

645 **Statistical analyses**

646 Statistical tests were performed using GraphPad Prism (v 10.0.3), using the scipy stat module (v 1.12), and
647 R (v 4.3.2). Statistical significance was assessed using Mann-Whitney two-tailed U test or two-tailed
648 Student's t test and threshold for considering an effect significant was 0.05, unless stated otherwise.
649

650 **Supplementary Figures**

651 **Figure S1**

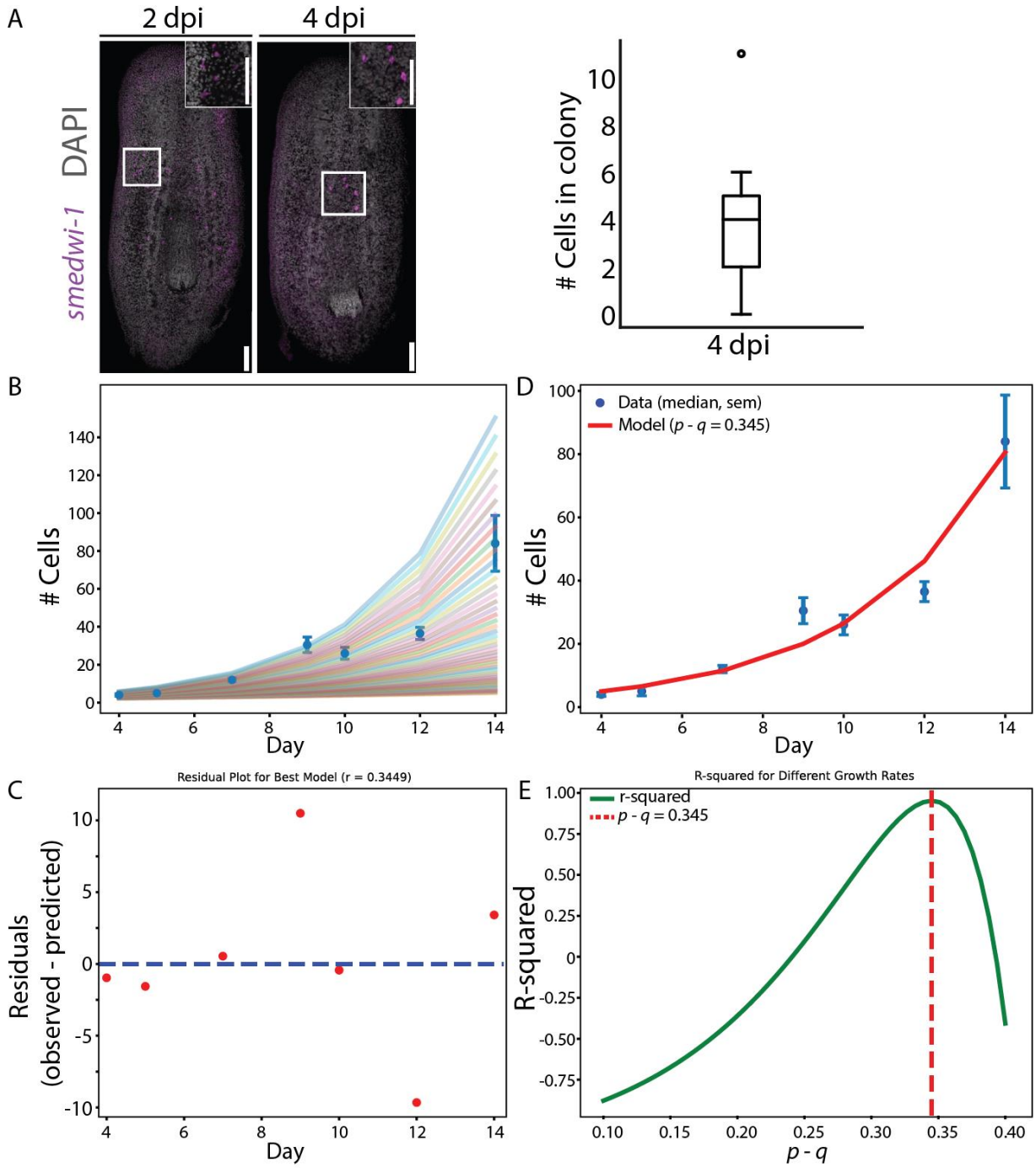

652

653 **Figure S1. Analysis of colony growth. (A) Shown are FISH images for detecting neoblasts (*smedwi-1*⁺; magenta) at 2 and 4 days**
654 **post irradiation (dpi), left and right, respectively. Colonies were not found at 2 dpi, and instead isolated *smedwi-1*+ were**
655 **scattered in the planarian parenchyma. At 4 dpi, single neoblasts already established small colonies (median = 4 cells;**

656 **quantification shown on right). (B-E) The effect of different growth parameters on colony size. (B) Shown are colony sizes when**
657 **considering a range of *q* values (0.1 - 0.4) with the experimentally determined *p* = 0.5. Data collected here and in published**
658 **analyses of colony sizes (Raz et al., 2021; Wagner et al., 2012) is shown as median (blue dots, and standard error of the mean).**
659 **(C) Shown is the best predicted fit growth following colony establishment using the exponential growth equation. (D) Analysis**
660 **of residuals between observed and predicted colony sizes using the best fitting parameters. (E) Shown is the r-squared**
661 **difference between observed and predicted data at a range of growth parameters. The minimal r-squared value is indicated**
662 **by the red dashed line.**

663 **Figure S2**

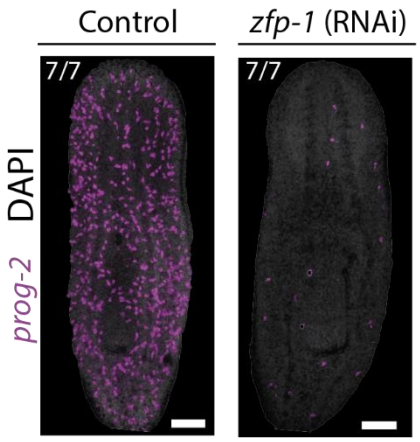

664

665 **Figure S2. Inhibition of epidermal progenitors by a single *zfp-1* dsRNA injection. Inhibition of *zfp-1* resulted in complete ablation**
666 **of epidermal progenitor production as observed by labeling animals with the epidermal progenitor marker, *prog-2*.**

667

668 **Figure S3**

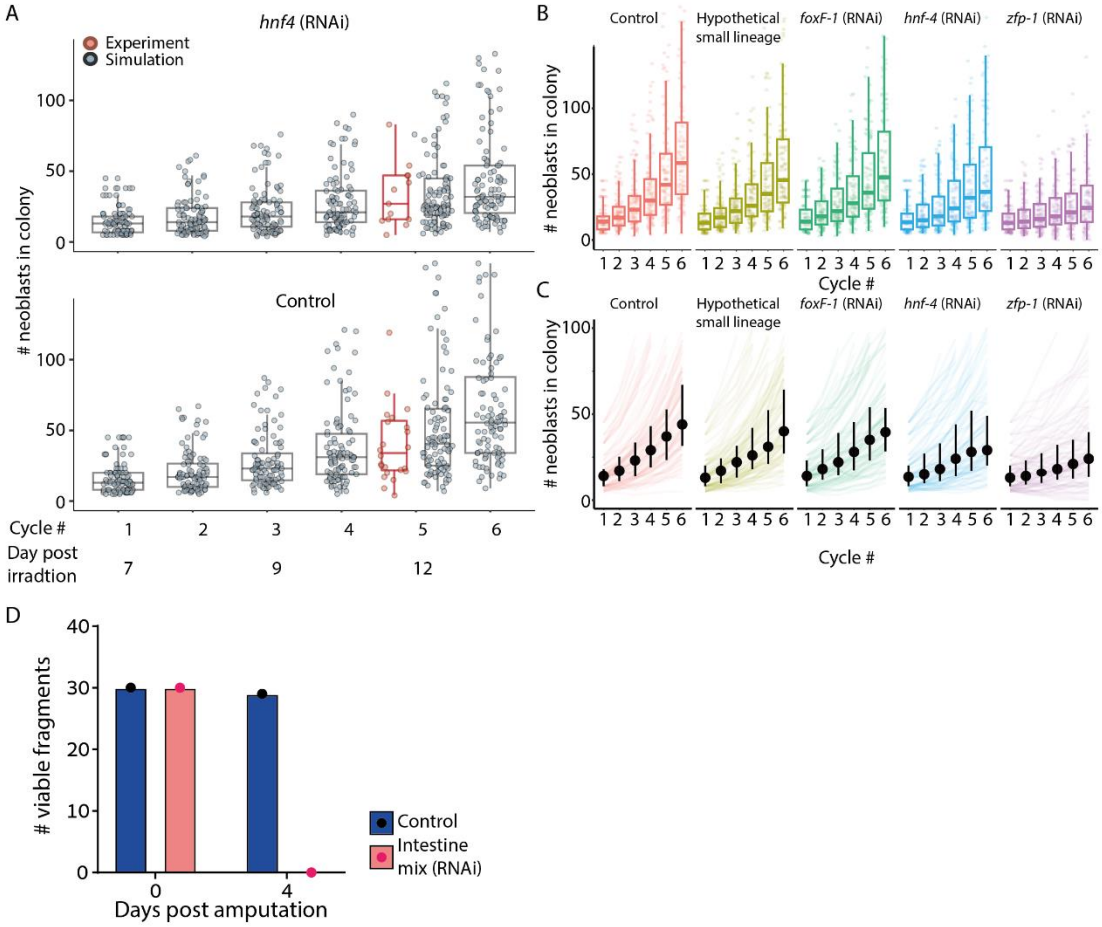

669

670 **Figure S3. Simulation of colony size following RNAi. (A) Simulation (gray) and comparison to experimental data (red) of**
671 **neoblast colonies in control and *hnf-4* (RNAi) animals. The simulation indicates that given the variability in colony size,**
672 **detecting significant differences in colony size is unlikely for this lineage. Each dot represents a single simulation (gray) or an**
673 **experimentally determined size (red). (B-C) Simulations of colony sizes over 6 cycles of replication starting approximately at**
674 **day seven post irradiation. (B) Boxplots showing the distribution of colony sizes (horizontal line, median; box, interquartile**
675 **range (IQR); vertical line, 99% range). Each dot represents a single simulation. (C) Simulation of colony growth (line) shows**
676 **growth over time (dot, median; vertical line, IQR). (D) The RNAi efficacy was evaluated through assessment of viability of**
677 **fragments obtained from animals following a single feeding of dsRNA that targeted intestine FSTFs (*hnf-4, gata4/5/6, nkx2.2*),**
678 **compared to a non-targeting control dsRNA (*unc22*). All fragments derived from worms fed with dsRNA targeting intestine**
679 **FSTFs died within four days post-feeding, demonstrating that a single dsRNA feeding induced a robust effect.**

680

681

682 **Supplementary Tables**

683 **Table S1**

684 Table S1. Downregulated genes in G2/M neoblasts following *zfp-1* (RNAi)

685 **Table S2**

686 Table S2. Upregulated genes in G2/M neoblasts following *zfp-1* (RNAi)

687 **Table S3**

688 Table S3. Downregulated genes in tissues or blastema following *zfp-1* (RNAi)

689 **Table S4**

690 Table S4. Upregulated genes in tissues or blastema following *zfp-1* (RNAi)

691 **Table S5**

692 Table S5. Summary of data extraction using WebPlotDigitizer

693 **Author contributions**

694 T.F. and O.W. designed the project. T.F. performed all experiments with support from P.V.C, Y.Y., and
695 S.D.. T.F. performed microscopy and imaging analysis. O.W. performed simulations and RNAseq data
696 analysis. T.F. and O.W. wrote and edited the manuscript.

697 **Declaration of Interests**

698 The authors declare no competing interests.

699 **Acknowledgements**

700 We thank Prof. David Sprinzak, Prof. Iftach Nachman, and Dr. Yasmine Meroz for their critical input. We
701 thank Shrey Jain for his assistance with performing FISH. We thank members of the Wurtzel lab for
702 feedback and discussions. We thank Dr. Daria Makarovsky from the interdepartmental services at Tel Aviv
703 University's Faculty of Medicine for assistance with gamma irradiation. O.W. is supported by the Israel

Science Foundation (grant 2039/18) and the European Research Council (no. 853640). O.W. is a Zuckerman Faculty Scholar.

References

Abkowitz JL, Golinelli D, Harrison DE, Guttorp P. 2000. In vivo kinetics of murine hemopoietic stem cells. *Blood* **96**:3399–3405. doi:10.1182/blood.V96.10.3399

Adler CE, Sánchez Alvarado A. 2015. Types or states? cellular dynamics and regenerative potential. *Trends Cell Biol* **25**:687–696. doi:10.1016/j.tcb.2015.07.008

Baguñà J. 2012. The planarian neoblast: the rambling history of its origin and some current black boxes. *Int J Dev Biol* **56**:19–37. doi:10.1387/ijdb.113463jb

Becker KA, Ghule PN, Therrien JA, Lian JB, Stein JL, van Wijnen AJ, Stein GS. 2006. Self-renewal of human embryonic stem cells is supported by a shortened G1 cell cycle phase. *J Cell Physiol* **209**:883–893. doi:10.1002/jcp.20776

Bohr TE, Shiroor DA, Adler CE. 2021. Planarian stem cells sense the identity of the missing pharynx to launch its targeted regeneration. *eLife* **10**. doi:10.7554/eLife.68830

Chan A, Ma S, Pearson BJ, Chan D. 2021. Collagen IV differentially regulates planarian stem cell potency and lineage progression. *Proc Natl Acad Sci USA* **118**. doi:10.1073/pnas.2021251118

Cheng L-C, Tu KC, Seidel CW, Robb SMC, Guo F, Sánchez Alvarado A. 2018. Cellular, ultrastructural and molecular analyses of epidermal cell development in the planarian *Schmidtea mediterranea*. *Dev Biol* **433**:357–373. doi:10.1016/j.ydbio.2017.08.030

Choi HMT, Schwarzkopf M, Fornace ME, Acharya A, Artavanis G, Stegmaier J, Cunha A, Pierce NA. 2018. Third-generation in situ hybridization chain reaction: multiplexed, quantitative, sensitive, versatile, robust. *Development* **145**. doi:10.1242/dev.165753

Currie KW, Molinaro AM, Pearson BJ. 2016. Neuronal sources of *hedgehog* modulate neurogenesis in the adult planarian brain. *eLife* **5**. doi:10.7554/eLife.19735

Dagan Y, Yesharim Y, Bonneau AR, Frankovits T, Schwartz S, Reddien PW, Wurtzel O. 2022. m6A is required for resolving progenitor identity during planarian stem cell differentiation. *EMBO J* **41**:e109895. doi:10.15252/embj.2021109895

Drevon D, Fursa SR, Malcolm AL. 2017. Intercoder reliability and validity of webplotdigitizer in extracting graphed data. *Behav Modif* **41**:323–339. doi:10.1177/0145445516673998

Eisenhoffer GT, Kang H, Sánchez Alvarado A. 2008. Molecular analysis of stem cells and their descendants during cell turnover and regeneration in the planarian *Schmidtea mediterranea*. *Cell Stem Cell* **3**:327–339. doi:10.1016/j.stem.2008.07.002

Fan Y, Chai C, Li P, Zou X, Ferrell JE, Wang B. 2023. Ultrafast distant wound response is essential for whole-body regeneration. *Cell* **186**:3606-3618.e16. doi:10.1016/j.cell.2023.06.019

Ferraro F, Celso CL, Scadden D. 2010. Adult stem cells and their niches. *Adv Exp Med Biol* **695**:155–168. doi:10.1007/978-1-4419-7037-4_11

741 Fincher CT, Wurtzel O, de Hoog T, Kravarik KM, Reddien PW. 2018. Cell type transcriptome atlas for the
742 planarian *Schmidtea mediterranea*. *Science* **360**. doi:10.1126/science.aaq1736

743 Forsthoefel DJ, James NP, Escobar DJ, Stary JM, Vieira AP, Waters FA, Newmark PA. 2012. An RNAi
744 screen reveals intestinal regulators of branching morphogenesis, differentiation, and stem cell
745 proliferation in planarians. *Dev Cell* **23**:691–704. doi:10.1016/j.devcel.2012.09.008

746 Gaviño MA, Reddien PW. 2011. A *Bmp/Admp* regulatory circuit controls maintenance and regeneration
747 of dorsal-ventral polarity in planarians. *Curr Biol* **21**:294–299. doi:10.1016/j.cub.2011.01.017

748 González-Estévez C, Felix DA, Rodríguez-Esteban G, Aboobaker AA. 2012. Decreased neoblast progeny
749 and increased cell death during starvation-induced planarian degrowth. *Int J Dev Biol* **56**:83–91.
750 doi:10.1387/ijdb.113452cg

751 Hayashi T, Asami M, Higuchi S, Shibata N, Agata K. 2006. Isolation of planarian X-ray-sensitive stem cells
752 by fluorescence-activated cell sorting. *Dev Growth Differ* **48**:371–380. doi:10.1111/j.1440-
753 169X.2006.00876.x

754 Hoffman M, Wurtzel O. 2023. PLANAtools-An interactive gene expression repository for the planarian
755 *Schmidtea mediterranea*. *Front Cell Dev Biol* **11**:1149537. doi:10.3389/fcell.2023.1149537

756 King RS, Newmark PA. 2018. Whole-Mount In Situ Hybridization of Planarians. *Methods Mol Biol*
757 **1774**:379–392. doi:10.1007/978-1-4939-7802-1_12

758 King RS, Newmark PA. 2013. In situ hybridization protocol for enhanced detection of gene expression in
759 the planarian *Schmidtea mediterranea*. *BMC Dev Biol* **13**:8. doi:10.1186/1471-213X-13-8

760 Lei K, Thi-Kim Vu H, Mohan RD, McKinney SA, Seidel CW, Alexander R, Gotting K, Workman JL, Sánchez
761 Alvarado A. 2016. *Egf* signaling directs neoblast repopulation by regulating asymmetric cell division in
762 planarians. *Dev Cell* **38**:413–429. doi:10.1016/j.devcel.2016.07.012

763 Levin M, Pietak AM, Bischof J. 2019. Planarian regeneration as a model of anatomical homeostasis:
764 Recent progress in biophysical and computational approaches. *Semin Cell Dev Biol* **87**:125–144.
765 doi:10.1016/j.semcdb.2018.04.003

766 Li L, Xie T. 2005. Stem cell niche: structure and function. *Annu Rev Cell Dev Biol* **21**:605–631.
767 doi:10.1146/annurev.cellbio.21.012704.131525

768 LoCascio SA, Lapan SW, Reddien PW. 2017. Eye Absence Does Not Regulate Planarian Stem Cells during
769 Eye Regeneration. *Dev Cell* **40**:381-391.e3. doi:10.1016/j.devcel.2017.02.002

770 Mangel M, Bonsall MB, Aboobaker A. 2016. Feedback control in planarian stem cell systems. *BMC Syst*
771 *Biol* **10**:17. doi:10.1186/s12918-016-0261-8

772 Molinaro AM, Lindsay-Mosher N, Pearson BJ. 2021. Identification of TOR-responsive slow-cycling
773 neoblasts in planarians. *EMBO Rep* **22**:e50292. doi:10.15252/embr.202050292

774 Morrison SJ, Spradling AC. 2008. Stem cells and niches: mechanisms that promote stem cell
775 maintenance throughout life. *Cell* **132**:598–611. doi:10.1016/j.cell.2008.01.038

776 Passegué E, Jamieson CHM, Ailles LE, Weissman IL. 2003. Normal and leukemic hematopoiesis: are
777 leukemias a stem cell disorder or a reacquisition of stem cell characteristics? *Proc Natl Acad Sci USA*
778 **100 Suppl 1**:11842–11849. doi:10.1073/pnas.2034201100

779 Pearson BJ, Sánchez Alvarado A. 2010. A planarian *p53* homolog regulates proliferation and self-renewal
780 in adult stem cell lineages. *Development* **137**:213–221. doi:10.1242/dev.044297

781 Pearson BJ. 2022. Finding the potency in planarians. *Commun Biol* **5**:970. doi:10.1038/s42003-022-
782 03905-9

783 Pellettieri J. 2010. Cell death and tissue remodeling in planarian regeneration. *Dev Biol*.

784 Petersen CP, Reddien PW. 2008. *Smed-betacatenin-1* is required for anteroposterior blastema polarity in
785 planarian regeneration. *Science* **319**:327–330. doi:10.1126/science.1149943

786 Raz AA, Wurtzel O, Reddien PW. 2021. Planarian stem cells specify fate yet retain potency during the cell
787 cycle. *Cell Stem Cell* **28**:1307-1322.e5. doi:10.1016/j.stem.2021.03.021

788 Reddien PW, Bermange AL, Murfitt KJ, Jennings JR, Sánchez Alvarado A. 2005a. Identification of genes
789 needed for regeneration, stem cell function, and tissue homeostasis by systematic gene perturbation
790 in planaria. *Dev Cell* **8**:635–649. doi:10.1016/j.devcel.2005.02.014

791 Reddien PW, Oviedo NJ, Jennings JR, Jenkin JC, Sánchez Alvarado A. 2005b. SMEDWI-2 is a PIWI-like
792 protein that regulates planarian stem cells. *Science* **310**:1327–1330. doi:10.1126/science.1116110

793 Reddien PW. 2018. The cellular and molecular basis for planarian regeneration. *Cell* **175**:327–345.
794 doi:10.1016/j.cell.2018.09.021

795 Reddien PW. 2013. Specialized progenitors and regeneration. *Development* **140**:951–957.
796 doi:10.1242/dev.080499

797 Rouhana L, Weiss JA, Forsthoefel DJ, Lee H, King RS, Inoue T, Shibata N, Agata K, Newmark PA. 2013.
798 RNA interference by feeding in vitro-synthesized double-stranded RNA to planarians: methodology
799 and dynamics. *Dev Dyn* **242**:718–730. doi:10.1002/dvdy.23950

800 Rueden CT, Schindelin J, Hiner MC, DeZonia BE, Walter AE, Arena ET, Eliceiri KW. 2017. ImageJ2: ImageJ
801 for the next generation of scientific image data. *BMC Bioinformatics* **18**:529. doi:10.1186/s12859-017-
802 1934-z

803 Salvetti A, Rossi L, Bonuccelli L, Lena A, Pugliesi C, Rainaldi G, Evangelista M, Gremigni V. 2009. Adult
804 stem cell plasticity: neoblast repopulation in non-lethally irradiated planarians. *Dev Biol* **328**:305–314.
805 doi:10.1016/j.ydbio.2009.01.029

806 Sandmann T, Vogg MC, Owlarn S, Boutros M, Bartscherer K. 2011. The head-regeneration transcriptome
807 of the planarian *Schmidtea mediterranea*. *Genome Biol* **12**:R76. doi:10.1186/gb-2011-12-8-r76

808 Scimone ML, Kravarik KM, Lapan SW, Reddien PW. 2014. Neoblast specialization in regeneration of the
809 planarian *Schmidtea mediterranea*. *Stem Cell Reports* **3**:339–352. doi:10.1016/j.stemcr.2014.06.001

810 Scimone ML, Meisel J, Reddien PW. 2010. The Mi-2-like *Smed-CHD4* gene is required for stem cell
811 differentiation in the planarian *Schmidtea mediterranea*. *Development* **137**:1231–1241.
812 doi:10.1242/dev.042051

813 Scimone ML, Wurtzel O, Malecek K, Fincher CT, Oderberg IM, Kravarik KM, Reddien PW. 2018. *foxF-1*
814 Controls Specification of Non-body Wall Muscle and Phagocytic Cells in Planarians. *Curr Biol* **28**:3787-
815 3801.e6. doi:10.1016/j.cub.2018.10.030

816 Singh SR, Burnicka-Turek O, Chauhan C, Hou SX. 2011. Spermatogonial stem cells, infertility and
817 testicular cancer. *J Cell Mol Med* **15**:468–483. doi:10.1111/j.1582-4934.2010.01242.x

818 Steele VE, Lange CS. 1976. Effects of irradiation on stem cell response to differentiation inhibitors in the
819 planarian *Dugesia etrusca*. *Radiat Res* **67**:21–29.

820 Tasaki J, Shibata N, Nishimura O, Itomi K, Tabata Y, Son F, Suzuki N, Araki R, Abe M, Agata K, Umesono Y.
821 2011. ERK signaling controls blastema cell differentiation during planarian regeneration. *Development*
822 **138**:2417–2427. doi:10.1242/dev.060764

823 Tu KC, Cheng L-C, T K Vu H, Lange JJ, McKinney SA, Seidel CW, Sánchez Alvarado A. 2015. *Egr-5* is a post-
824 mitotic regulator of planarian epidermal differentiation. *eLife* **4**:e10501. doi:10.7554/eLife.10501

825 Van Roten A, Barakat AZA-Z, Wouters A, Tran TA, Mouton S, Noben J-P, Gentile L, Smeets K. 2018. A
826 carcinogenic trigger to study the function of tumor suppressor genes in *Schmidtea mediterranea*. *Dis*
827 *Model Mech* **11**. doi:10.1242/dmm.032573

828 van Wolfswinkel JC, Wagner DE, Reddien PW. 2014. Single-cell analysis reveals functionally distinct
829 classes within the planarian stem cell compartment. *Cell Stem Cell* **15**:326–339.
830 doi:10.1016/j.stem.2014.06.007

831 Wagner DE, Ho JJ, Reddien PW. 2012. Genetic regulators of a pluripotent adult stem cell system in
832 planarians identified by RNAi and clonal analysis. *Cell Stem Cell* **10**:299–311.
833 doi:10.1016/j.stem.2012.01.016

834 Wagner DE, Wang IE, Reddien PW. 2011. Clonogenic neoblasts are pluripotent adult stem cells that
835 underlie planarian regeneration. *Science* **332**:811–816. doi:10.1126/science.1203983

836 Wang IE, Wagner DE, Reddien PW. 2018. Clonal Analysis of Planarian Stem Cells by Subtotal Irradiation
837 and Single-Cell Transplantation. *Methods Mol Biol* **1774**:479–495. doi:10.1007/978-1-4939-7802-1_20

838 Wenemoser D, Lapan SW, Wilkinson AW, Bell GW, Reddien PW. 2012. A molecular wound response
839 program associated with regeneration initiation in planarians. *Genes Dev* **26**:988–1002.
840 doi:10.1101/gad.187377.112

841 Wenemoser D, Reddien PW. 2010. Planarian regeneration involves distinct stem cell responses to
842 wounds and tissue absence. *Dev Biol* **344**:979–991. doi:10.1016/j.ydbio.2010.06.017

843 Wurtzel O, Cote LE, Poirier A, Satija R, Regev A, Reddien PW. 2015. A Generic and Cell-Type-Specific
844 Wound Response Precedes Regeneration in Planarians. *Dev Cell* **35**:632–645.
845 doi:10.1016/j.devcel.2015.11.004

846 Wurtzel O, Oderberg IM, Reddien PW. 2017. Planarian Epidermal Stem Cells Respond to Positional Cues
847 to Promote Cell-Type Diversity. *Dev Cell* **40**:491-504.e5. doi:10.1016/j.devcel.2017.02.008

848 Zeng A, Li H, Guo L, Gao X, McKinney S, Wang Y, Yu Z, Park J, Semerad C, Ross E, Cheng L-C, Davies E, Lei
849 K, Wang W, Perera A, Hall K, Peak A, Box A, Sánchez Alvarado A. 2018. Prospectively isolated
850 Tetraspanin+ neoblasts are adult pluripotent stem cells underlying planaria regeneration. *Cell*
851 **173**:1593-1608.e20. doi:10.1016/j.cell.2018.05.006

852 Zhu SJ, Hallows SE, Currie KW, Xu C, Pearson BJ. 2015. A *mex3* homolog is required for differentiation
853 during planarian stem cell lineage development. *eLife* **4**. doi:10.7554/eLife.07025